

Photon-counting Detector CT with Deep Learning Noise Reduction to Detect Multiple Myeloma

Francis I. Baffour, MD • Nathan R. Huber, PhD • Andrea Ferrero, PhD • Kishore Rajendran, PhD • Katrina N. Glazebrook, MB, ChB • Nicholas B. Larson, MS, PhD • Shaji Kumar, MD • Joselle M. Cook, MBBS • Shuai Leng, PhD • Elisabeth R. Shanblatt, PhD • Cynthia H. McCollough, PhD • Joel G. Fletcher, MD

From the Department of Radiology (F.I.B., N.R.H., A.F., K.R., K.N.G., S.L., C.H.M., J.G.F.), Division of Biomedical Statistics and Informatics, Department of Quantitative Health Sciences (N.B.L.), and Division of Hematology, Department of Medicine (S.K., J.M.C.), Mayo Clinic, 200 First St SW, Rochester, MN 55905; and Siemens Medical Solutions USA, Malvern, Pa (E.R.S.). Received February 9, 2022; revision requested April 4; revision received June 15; accepted July 18. **Address correspondence** to F.I.B. (email: baffour.francis@mayo.edu).

Study supported by Siemens Healthineers, which owns the evaluated system under the terms of a sponsored research agreement with the Mayo Clinic. Study supported by the National Institutes of Health (R01 EB028590); study supported by the Mayo Clinic Graduate School of Biomedical Science.

Conflicts of interest are listed at the end of this article.

Radiology 2022; 000:1–8 • <https://doi.org/10.1148/radiol.220311> • Content codes: 

Background: Photon-counting detector (PCD) CT and deep learning noise reduction may improve spatial resolution at lower radiation doses compared with energy-integrating detector (EID) CT.

Purpose: To demonstrate the diagnostic impact of improved spatial resolution in whole-body low-dose CT scans for viewing multiple myeloma by using PCD CT with deep learning denoising compared with conventional EID CT.

Materials and Methods: Between April and July 2021, adult participants who underwent a whole-body EID CT scan were prospectively enrolled and scanned with a PCD CT system in ultra-high-resolution mode at matched radiation dose (8 mSv for an average adult) at an academic medical center. EID CT and PCD CT images were reconstructed with Br44 and Br64 kernels at the 2-mm section thickness. PCD CT images were also reconstructed with Br44 and Br76 kernels at 0.6-mm section thickness. The thinner PCD CT images were denoised by using a convolutional neural network. Image quality was objectively quantified in two phantoms and a randomly selected subset of participants (10 participants; median age, 63.5 years; five men). Two radiologists scored PCD CT images relative to EID CT by using a five-point Likert scale to detect findings reflecting multiple myeloma. The scoring for the matched reconstruction series was blinded to scanner type. Reader-averaged scores were tested with the null hypothesis of equivalent visualization between EID and PCD.

Results: Twenty-seven participants (median age, 68 years; IQR, 61–72 years; 16 men) were included. The blinded assessment of 2-mm images demonstrated improvement in viewing lytic lesions, intramedullary lesions, fatty metamorphosis, and pathologic fractures for PCD CT versus EID CT ($P < .05$ for all comparisons). The 0.6-mm PCD CT images with convolutional neural network denoising also demonstrated improvement in viewing all four pathologic abnormalities and detected one or more lytic lesions in 21 of 27 participants compared with the 2-mm EID CT images ($P < .001$).

Conclusion: Ultra-high-resolution photon-counting detector CT improved the visibility of multiple myeloma lesions relative to energy-integrating detector CT.

© RSNA, 2022

Online supplemental material is available for this article.

Bone disease is common in multiple myeloma, with approximately 80% of patients developing bone lesions throughout the course of disease (1). CT is sensitive in detecting osteolytic lesions (2,3). Therefore, the International Myeloma Working Group recommends low-dose whole-body CT as the imaging test to evaluate lytic bone disease (4–6) because of its high sensitivity and specificity. According to International Myeloma Working Group recommendations, the detection at radiography or CT of a single lytic lesion larger than 5 mm is sufficient for a diagnosis of multiple myeloma and initiation of treatment even if the patient is asymptomatic. When disease relapse is suspected, whole-body low-dose CT is again recommended to assess changes in osteolytic disease burden and guide retreatment (4). Patients typically undergo several CT scans over the course of this disease.

Currently, clinically acceptable whole-body low-dose CT protocols have a mean effective dose ranging between 4 mSv and 8 mSv, depending on patient size and scanner technology (7). This dose range is adequate in detecting osteolytic bone disease. However, low-dose images also have substantial image noise, resulting in lower quality images. Specifically, for whole-body low-dose CT, both soft tissue and bone resolution are limited relative to full-dose CT images (5). Improvements in spatial resolution can be achieved with either higher doses, for example by using grid-based attenuators to reduce the effective detector pixel size (8) or by using CT systems with intrinsically higher spatial resolution such as scanners equipped with photon-counting detectors (PCDs) (9,10).

The smaller detector pixel sizes used in PCD CT systems eliminate the need for high-spatial-resolution comb

Abbreviations

EID = energy-integrating detector, PCD = photon-counting detector

Summary

Photon-counting detector CT in ultra-high-resolution mode with and without a deep learning noise reduction algorithm was superior in viewing multiple myeloma lesions compared with energy-integrating detector CT.

Key Results

- In a prospective study of 27 adult participants with multiple myeloma, photon-counting detector (PCD) CT outperformed energy-integrating detector (EID) CT at viewing lytic lesions, intramedullary lesions, and fatty metamorphosis ($P < .001$).
- High-resolution (PCD) CT with deep learning noise reduction detected more lytic lesions relative to EID CT (at least one additional lesion in 21 of 27 participants; $P < .001$).

or grid filters, leading to increased dose efficiency (11). Recently, a clinical whole-body PCD system demonstrated superior resolution (125- μm in-plane resolution) and better noise properties (up to 47% lower noise) compared with conventional energy-integrating detector (EID) CT at the same radiation dose (12).

In whole-body low-dose CT, the primary clinical need is to improve the evaluation of skeletal findings while maintaining an acceptably low radiation dose to mitigate concerns about radiation risk from repeated scans. At these low doses, PCD CT is more likely to improve visualization of features of myeloma compared with EID CT. The purpose of our study was to demonstrate the diagnostic impact of improved spatial resolution in whole-body low-dose CT scans to view multiple myeloma by

using PCD CT with advanced deep learning postprocessing, and compare these findings to conventional EID CT.

Materials and Methods

Siemens Healthineers provided the PCD CT system in a research agreement with Mayo Clinic. All data in our study were acquired and controlled by authors employed by Mayo Clinic who did not receive financial support from Siemens.

Our prospective study was approved by our institutional review board (Mayo Clinic; Rochester, Minn). Written informed consent was obtained from participants.

Study Participants

Participants aged 18 years and older with known or suspected multiple myeloma undergoing clinically indicated whole-body low-dose CT were enrolled in this study between April 2021 and July 2021 at a single academic medical center (Fig 1). Participants first underwent an EID CT examination and subsequently underwent a same-day PCD CT scan at a matched radiation dose.

EID CT and PCD CT Low-dose Whole-body CT Protocols

Scan parameters are summarized in Table 1. Whole-body low-dose EID CT at our institution involves a single examination from above the raised elbows through the knees. Two image series are reconstructed: body regular (Br), Br44 kernel for bone marrow and soft-tissue evaluation, and a sharp-kernel (Br64) series to evaluate osseous structures.

The PCD CT system (Naeotom Alpha, VA40; Siemens Healthineers) was operated in ultra-high-resolution mode (120 mm \times 0.2 mm collimation, 0.151 mm \times 0.176 mm

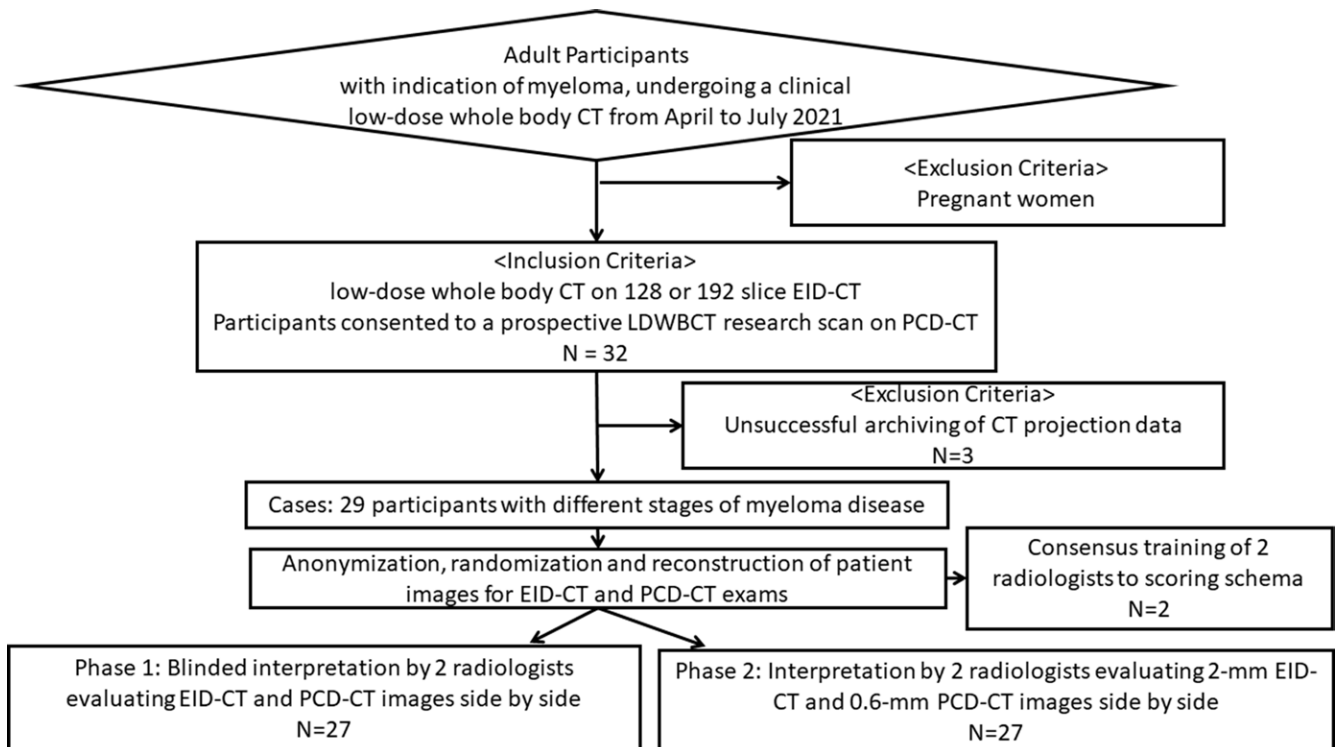


Figure 1: Study inclusion and exclusion flowchart. EID = energy-integrating detector, PCD = photon-counting detector.

Table 1: Acquisition and Reconstruction Parameters

Parameter	EID CT	PCD CT
Acquisition		
Scanner model name	Edge/Edge+, Alpha Force	
Tube potential (kV)	120	120
AEC parameter	70 QRM	64 CarekEV IQ
Collimation (mm)	120 × 0.2	
Edge/Edge+	128 × 0.6	
Force	192 × 0.6	
Rotation time (sec)	0.5	0.25
Pitch	1	0.85
Average CTDI _{vol} (mGy)	4	4
DLP (mGy · cm)	517	424
Energy threshold (keV)	NA	20
Reconstruction		
Phase 1		
Section width (mm)	2	2
Increment (mm)	1	1
Soft tissue kernel	Br44	Br44
Bone kernel	Br64	Br64
Matrix	512 × 512	512 × 512
Reconstruction algorithm	ADMIRE	QIR
Strength	3	3
Phase 2		
Section width (mm)	2	0.6
Increment (mm)	1	0.5
Soft tissue kernel	Br44	Br44
Bone kernel	Br64	Br76
Matrix size (pixels)	512 × 512	1024 × 1024
Reconstruction algorithm	ADMIRE	QIR-off, CNN
Strength	3	

Note.—ADMIRE = advanced modeled iterative reconstruction, AEC = automatic exposure control, CNN = convolutional neural network, CTDI_{vol} = volume CT dose index, DLP = dose-length product, EID = energy-integrating detector, IQ = image quality, NA = not applicable, PCD = photon counting detector, QIR = quantum iterative reconstruction, QRM = quality reference effective milliamperere-seconds.

detector pixel size at isocenter) at a radiation dose matched to the EID CT scan. PCD CT and EID CT images were reconstructed with matching section thickness (2 mm) and reconstruction kernels (Br44, Br64) for side-by-side comparison. Subsequently, PCD CT images were reconstructed by using the smooth kernel (Br44) and a sharper kernel (Br76) at 0.6-mm section thickness, with quantum iterative reconstruction disabled, and processed using a generalizable noise and artifact reduction convolutional neural network (13). This facilitated a comparison between EID CT images (Br44 and Br64, 2-mm sections) and high-spatial-resolution PCD CT (Br44 and Br76, 0.6-mm sections).

Quantitative Assessment of Image Quality

Image quality for EID CT and PCD CT were evaluated by using phantom and patient images.

Table 2: Image Review Phase and Associated Scoring System

Image Review Task	Phase of Reader Study	Likert Scoring System
Lytic bone lesions	1, 2	A
Hyperdense nodular intramedullary soft-tissue lesion or lesions	1, 2	A
Fat attenuation of myeloma lesions	1, 2	A
Pathologic fractures	1, 2	A
Overall number of lytic lesions	2	B

Note.—Data represents the phase of the study during which the image review task was performed, and the Likert scoring system used. Likert score system A was scored as follows: -2, worse visualization and diagnostic confidence; -1, worse visualization with no change in diagnostic confidence; 0, equivalent visualization and diagnostic confidence; 1, improved visualization with no change in diagnostic confidence; 2, improved visualization and improved diagnostic confidence. B, Likert Scores as follows: -2, more than 5 missed lesions; -1, 1-5 missed lesions; 0, same number of lesions; +1, 1-5 additional lesions; +2, >5 additional lesions.

Phantom image quality assessment.—Phantom scans were performed using the same acquisition protocols as patient scans (Table 1). High-contrast spatial resolution (Br64/2-mm-section for EID CT and PCD CT, Br76/0.6-mm-section for PCD CT) were evaluated by using the American College of Radiology CT accreditation phantom (CT ACR-464; Sun Nuclear Corporation).

The three-dimensional noise power spectrum computed from water phantom scans was used to characterize image noise. The spatial frequencies corresponding to the peak and noise power spectrum quartile values were compared to assess noise texture differences between EID CT (Br64) and PCD CT (Br64, Br76).

Patient image quality assessment.—Line profiles through lytic bone lesions identified by one musculoskeletal radiologist (F.I.B.) were obtained from 10 randomly selected participants to assess spatial resolution differences in vivo. Bone lesion contrast was computed as the difference between the average peak values and the average of the valley of the lesion profile.

Noise was measured in triplicate as the CT number SD at five uniform regions (thoracic and abdominal aorta, liver, iliacus, and vastus lateralis) in the 10 participants.

Radiologist Assessment of Imaging Findings of Myeloma

Phase 1.—To compare PCD CT and EID CT with matched conditions (Br44 and Br64, 2-mm sections), two musculoskeletal radiologists (F.I.B. and K.N.G., with 3 and 29 years of experience, respectively) who were blinded to participant demographics, CT system, and scan protocols independently scored four multiple myeloma features on a five-point Likert scale that ranged from -2 to 2 (Table 2). Specifically, they evaluated features that determined myeloma activity (14-16): the skeleton for lytic lesions, the medullary cavity for focal hyperdense nodular soft-tissue lesions, fat attenuation in my-

Table 3: Patient Characteristics and Response Criteria

Parameter	Participants Included in the Reader Assessment (<i>n</i> = 27)
Participant characteristic	
Median age (y)*	68 (61–72)
Age range (y)	37–90
Disease	
Multiple myeloma	25/27 (93)
Smoldering multiple myeloma	1/27 (4)
Myeloma with primary amyloidosis	1/27 (4)
R-ISS	
I	4/11 (36)
II	5/11 (45)
III	2/11 (18)
Missing data	16/27 (59)
FISH risk category	
High risk	9/27 (33)
Standard risk	18/27 (67)
Response at time of scan	
Complete response	13/27 (48)
Very good partial response	2/27 (7)
Partial response	3/27 (11)
Stable disease	3/27 (11)
Progressive disease	6/27 (22)

Note.—Data are per the International Myeloma Working Group Uniform Response Criteria (17). Unless otherwise specified, data are numbers of participants; data in parentheses are percentages. FISH = fluorescence in situ hybridization, R-ISS = revised multiple myeloma international staging system.

* Data in parentheses are IQRs.

eloma lesions, and pathologic fractures. On a single-monitor clinical workstation, randomized axial images were presented in a two-by-two panel (top row: scanner 1, soft tissue and bone kernels; bottom row: scanner 2, soft tissue and bone kernels), where the top row was scored against the bottom row. Radiologists generated sagittal and coronal reformations and displayed them on a second monitor to evaluate the spine and appendicular skeleton for fractures. Before the blinded study, the radiologists reviewed two sample image sets (not included in the reader study) in consensus to get familiar with the scoring system. The final Likert scores were adjusted post hoc, and therefore positive scores reflected PCD CT preference relative to EID CT.

Phase 2.—Four weeks after phase 1, the same radiologists compared denoised PCD CT images (0.6-mm sections) with EID CT images (2-mm sections). Image blinding in this phase was not possible because of perceptible differences in image characteristics between the ultra-high-resolution PCD CT images and the EID CT images. The radiologists independently scored PCD CT images against EID CT images by using the same scoring system as in phase 1. In addition, a change in the number of detected lytic lesions for each participant was recorded (Table 2).

Statistical Analysis

For each phase, a one-sample two-sided Wilcoxon rank sum test was performed for each metric using reader-averaged scores per participant, with the null hypothesis corresponding to a median score of 0 (equivalent image appearance and diagnostic confidence between EID CT and PCD CT). Structurally missing data for each category because of the absence of relevant pathologic findings were excluded. Multiple testing was accounted for with a Holm correction of *P* values, and adjusted *P* values less than .05 were considered to indicate statistical significance. All data were analyzed by using statistical software (R v4.0.3, R Core Team; and Excel 365, Microsoft).

We approximated necessary sample size based on a two-sided one-sample Wilcoxon rank sum test by using software (PASS 2022; NCSS). With a conservative Bonferroni-adjusted α level of $.05/5 = .01$, accounting for number of assessments per study phase, the minimum necessary sample size for 90% power was 20 participants to identify a one-unit shift in rating scale assuming an underlying standard normal distribution.

Results

Study Participant Characteristics

Twenty-nine participants with known or suspected plasma cell dyscrasias underwent PCD CT after clinically indicated EID CT. The cohort size used in the blinded reader study was 27 participants (excluding the two participants used for consensus review). Demographics and disease status are summarized in Table 3 (17). The median participant age was 68 years (IQR, 61–72 years); 16 of 27 study participants were men. Objective image quality assessment was performed in 10 participants (median age, 63.5 years; five men).

Quantitative Assessment of Image Quality

Phantom image quality assessment.—The six-line-pair per centimeter bar pattern from the high-contrast spatial resolution module of the American College of Radiology CT accreditation phantom can be resolved with both EID CT and PCD CT reconstructions at 2-mm section thickness and Br64 kernel, whereas the PCD CT 0.6-mm-thick Br76 image showed the 10 line pair per centimeter bar pattern (Fig E1 [online]).

The area under the noise power spectrum profile was 8.3% lower (1159.6 HU² vs 1264.5 HU²) for the PCD CT versus the EID CT, respectively, at matched reconstruction parameters (Fig E2 [online]). The difference was particularly pronounced at low spatial frequencies. Moreover, the 0.6-mm-thick Br76 PCD CT reconstruction with convolutional neural network denoising demonstrated higher spatial frequencies (≤ 1.98 mm⁻¹ vs 0.99 mm⁻¹ on the Br64 reconstructions) and lower noise amplitude (66% decrease in the area under the noise power spectrum curve, 389.5 HU² vs 1159.6 HU², respectively) throughout the frequency spectrum, an improvement in image noise despite the thinner sections.

Patient image quality assessment.—Line profiles through representative bone lesions showed the average lesion contrast to be 38% (696 and 505 HU) and 54% (779 and 505 HU) higher

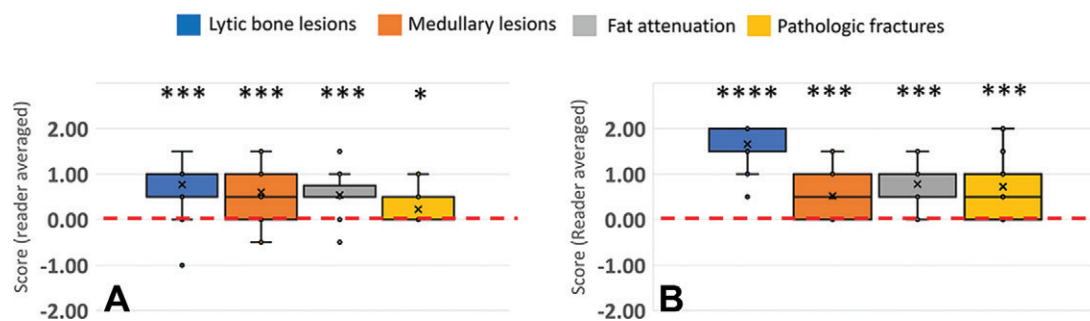


Figure 2: Box and whisker plots of reader-averaged scores for reader assessments in (A) phase 1 and (B) phase 2. Reader-averaged scores are presented on the vertical axis. A neutral score of zero is indicated by the horizontal dashed red line. A score of +1 (−1) indicates preference for the photon-counting detector (PCD) CT (energy-integrating detector [EID] CT) images, with no change in diagnostic confidence. A score of +2 (−2) indicates improved diagnostic confidence for the PCD CT (EID CT) images. Symbols above each assessment indicated Holm-adjusted significance level under a two-sided one-sample Wilcoxon rank sum test. * $P < .05$, ** $P < .01$, *** $P < .001$, **** $P < .0001$.

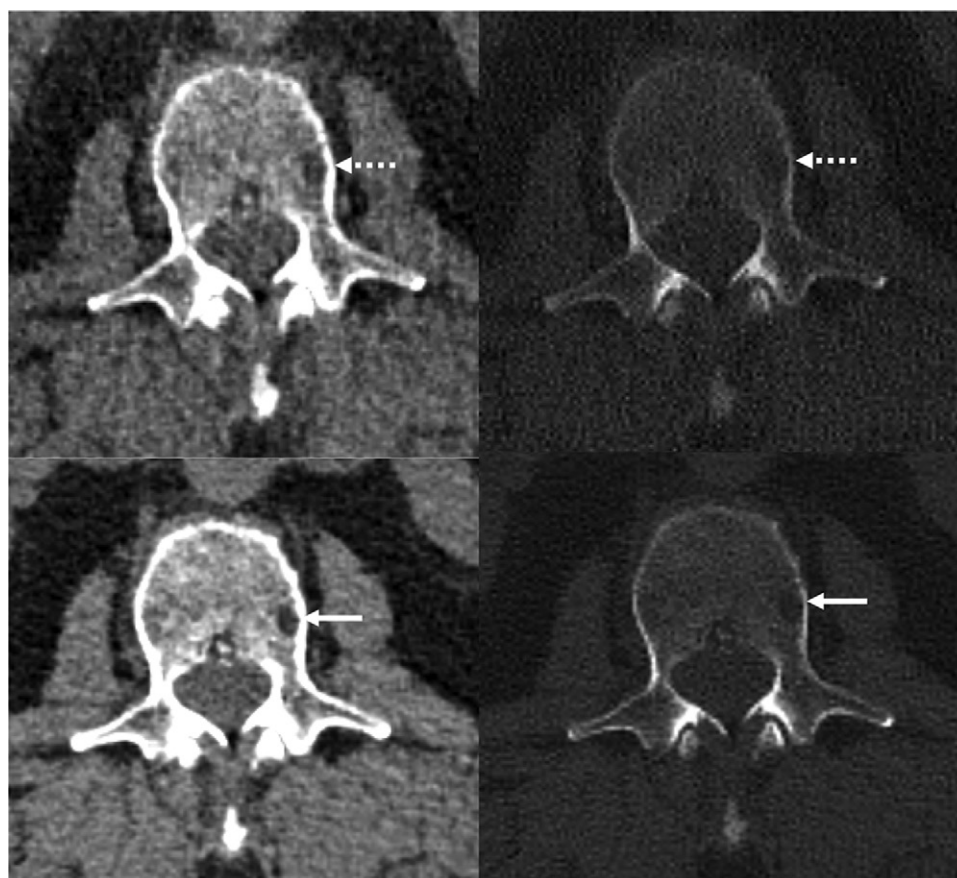


Figure 3: Reference protocol (top) and evaluated protocol (bottom) images in a 74-year-old man with multiple myeloma. The soft tissue reconstruction is shown (left side; window width, 400; window level, 40), whereas the right column is the bone reconstruction (right side; window width, 3700; window level, 600). A lytic bone lesion in the L3 vertebral body is more conspicuous on the noncontrast-enhanced axial photon-counting detector CT reconstruction images (bottom; solid arrows) compared with the noncontrast-enhanced axial energy-integrating detector CT reconstruction images (top; dashed arrows).

for 2-mm and 0.6-mm-thick PCD CT images relative to EID CT, respectively (Fig E3 [online]).

On average, there was 20% lower noise (66 HU for EID CT Br64, 53 HU for both PCD CT Br64 and Br76 with convolutional neural network) measured in the five anatomic locations on the PCD CT bone image series compared with EID CT (Fig E4 [online]).

Radiologist Assessment of Imaging Findings of Myeloma

Phase 1 Comparison of EID and PCD with matching reconstruction parameters.—The average scores for the two readers in the blinded review of EID CT and PCD CT images with matching reconstruction parameters (Br 44 and Br 64, 2-mm section thickness) are shown in Figure 2 and Figure E5 (online). There

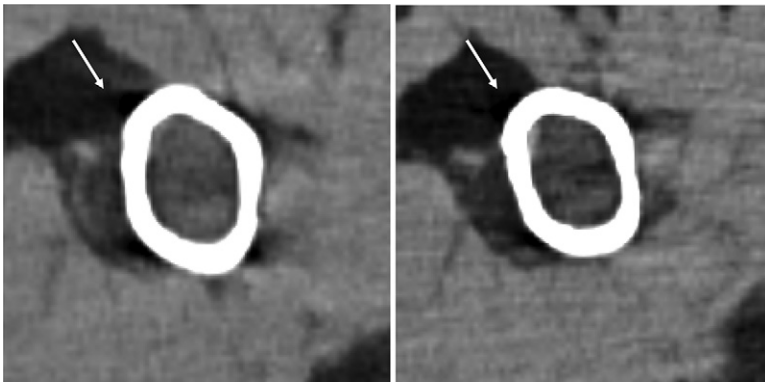


Figure 4: Images in a 71-year-old man with relapsed multiple myeloma, after autologous stem cell transplant, who was administered single-agent daratumumab maintenance therapy. Foci of intramedullary hyperattenuation in the left proximal humerus with macroscopic internal fat suggested fatty metamorphosis of a multiple myeloma lesion after therapy. The degree of fat infiltration is better appreciated on the noncontrast-enhanced axial photon-counting detector (PCD) CT image (right), compared with the noncontrast-enhanced axial energy-integrating detector CT image (left). Beam hardening artifact (arrows), notably along the anterior cortex of the proximal humerus, is reduced on the PCD CT image.

was improvement with PCD CT across all visualization assessments (Holm-adjusted $P < .001$), with the strongest differences observed for lytic bone lesions (median score, 1.0), nodular intramedullary lesions (median score, 0.5), and fat attenuation in myeloma lesions (median score, 0.5) (Figs 3, 4). The observed improvement in viewing pathologic fractures at PCD CT was moderate (median score, 0; $P = .03$).

Phase 2 Comparison of EID and PCD with different reconstruction parameters.—The average scores for the two readers in the unblinded review of 2-mm EID CT and 0.6-mm PCD images with convolutional neural network–based noise reduction are shown in Figure 2 and Figure E5 (online). There was improved viewing in detection of multiple myeloma features using the 0.6-mm PCD CT images ($P < .001$ for both Br44 and Br76 kernels) (Figs 5, 6), with the strongest differences observed for lytic bone lesions (median average score, 2.0) and fat attenuation in myeloma lesions (median average score, 1.0). Additionally, a higher overall number of depicted lytic lesions was observed ($P < .001$) on PCD CT images relative to EID CT images (21 of 27 participants; median average score, 1.5), with reader 1 and 2 identifying five or more lesions in 10 of 27 and 11 of 27 participants, respectively, on the 0.6-mm PCD CT images relative to the 2-mm EID CT images.

Discussion

Photon-counting detectors (PCDs) offer a dose-efficient approach to low-dose CT scanning with improved spatial resolution, which can improve visibility of myeloma bone disease. Results from our study suggest that a clinical PCD CT system operated in ultra-high-resolution acquisition mode (120 mm \times 0.2 mm) produces images with 23% (53 HU vs 69 HU) lower noise compared with conventional energy-integrating detector (EID) CT systems at matched radiation dose. The reduced noise, lytic lesions, intramedullary lesions, and fat attenuation were clearly viewed on images from the PCD CT compared with EID CT systems with matched reconstruction parameters (2-mm section thick-

ness: post hoc median Likert scores of 1.0, 0.5, and 0.5, respectively; $P < .001$) and with thinner PCD CT images (0.6-mm section thickness: post hoc median Likert scores of 2.0, 0.5, and 1.0, respectively; $P < .001$). Additionally, one or more lytic lesions were depicted on the thin-section PCD CT images in 21 of 27 participants (post hoc median Likert score, 1.5; $P < .001$).

Most conventional CT systems use detector pixels of 0.25–0.625 mm for routine imaging tasks. Further improvements in spatial resolution using smaller detector pixels are beneficial in musculoskeletal imaging to evaluate osseous structures. With improved spatial resolution, details about the integrity of cortical and trabecular bone are clearly depicted (18–20). Clinical CT systems use different methods to attain high spatial resolution. The use of sharper reconstruction kernels and thinner image sections can help increase image sharpness and reduce partial volume averaging, respectively. The use of attenuating comb filters (8) and advanced detector technology to assemble smaller detector pixels (21) can decrease the pixel aperture for ultra-high-spatial-resolution imaging; these approaches exhibit markedly reduced geometric radiation dose efficiency.

Unlike EIDs, PCDs do not require reflector material to constrain the light signal generated during x-ray conversion to the correct detector element. Rather, x-rays are directly converted to electric signals (electron-hole pairs) in the semiconductor material, which are then driven to the anode and cathode terminals by an applied voltage potential. As a result, they can be manufactured with a smaller detector pixel size without any loss in geometric dose efficiency. Without attenuating comb filters, PCD-based high-spatial-resolution imaging can be applied to any anatomic region. Large joints, such as the shoulders and pelvis, and the spine can be scanned using the ultra-high-resolution mode without the dose penalty encountered in the comb filter technique. The ultra-high-resolution mode in the PCD CT system evaluated in this study enables a section thickness of 0.2 mm and a maximum cutoff spatial frequency of 40 line-pairs per cm (in-plane), the highest reported so far for a clinical CT system (11,20). Using 0.15-mm detector pixel size (isocenter) for acquisition, PCD CT images reconstructed at a spatial resolution that is lower than the maximum intrinsic system resolution results in lower image noise than EID CT at the same spatial resolution (11). This noise reduction can be leveraged to generate thin image sections using PCD CT relative to EID CT to improve spatial resolution, or to reduce image noise at a spatial resolution matched to EID CT.

The PCD CT system investigated in our study allows the generation of high-spatial-resolution images for whole-body CT. However, improved image sharpness requires a trade-off between image noise and radiation dose. In this study, we demonstrated that the diagnostic performance of whole-body low-dose CT is significantly improved with the use of ultra-sharp reconstruction kernels, large image matrices, and sub-millimeter image sections. Additionally, these gains can be obtained without a higher radiation dose by using deep learning noise reduction

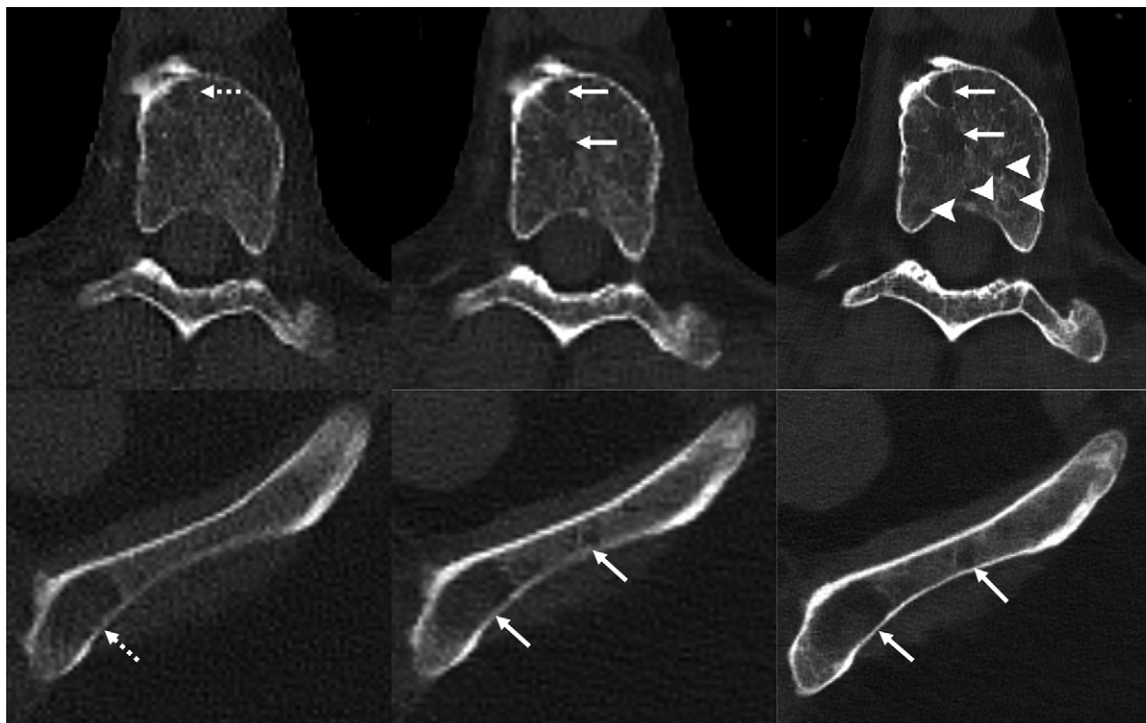


Figure 5: Images in a 71-year-old man with multiple myeloma. Lytic lesions (dashed arrows) within a thoracic vertebral body and the left iliac wing are more conspicuous on the noncontrast-enhanced axial photon-counting detector (PCD) CT image (middle; solid arrows) compared with noncontrast-enhanced axial energy-integrating detector CT image (left). With 0.6-mm Br76 noncontrast-enhanced axial PCD CT reconstruction images (right), more lesions were detected (arrowheads).



Figure 6: Images in a 60-year-old woman with multiple myeloma. Two-millimeter noncontrast-enhanced axial energy-integrating detector CT image (left), 2-mm noncontrast-enhanced axial photon-counting detector (PCD) CT image (center), and noncontrast-enhanced axial 0.6-mm PCD CT image (right) show representative pathologic myeloma-induced healing pathologic fracture through the lower sternum. Cortical irregularity is evident on all three reconstruction images; however, the associated callus is only visible on the 0.6-mm PCD CT reconstruction image (right; arrow).

techniques to offset the higher level of image noise associated with sharper and thinner reconstructions (Fig E6 [online]). Ultimately, use of the ultra-high-resolution PCD CT scan mode enables improved spatial resolution without a noise or dose penalty, which is particularly helpful for musculoskeletal imaging tasks. This was demonstrated in our study by the improved detection of lytic bone lesions.

Our study had certain limitations. First, the participants all had multiple myeloma at different stages of disease and therefore assessment of sensitivity and specificity to diagnose multiple myeloma by using the PCD CT system was not possible. Because an imaging standard of myelomatous lesions (ie, MRI) was not available, analyses could not be performed at the lesion level and were instead performed at the participant level. Second, the EID CT examinations were performed on scanners that were different models (Siemens Edge, Edge+, and

Force), albeit by using the same acquisition and reconstruction protocols. However, these EID CT scanners were from the same manufacturer and have similar performance. Third, although quantum iterative reconstruction algorithms are the standard reconstruction technique for this PCD CT and were used for image reconstruction in phase 1 (2-mm section thickness), because of substantial image noise associated with quantum iterative reconstruction at thinner image sections (0.6 mm), ultra-sharp reconstruction kernel and lower radiation dose, the generalizable noise and artifact reduction convolutional neural network was preferred for phase 2. For this reconstruction, the scanner was operated in quantum iterative reconstruction-off mode, with the inherent associated limitation of having only the minimally possible statistical optimization (22). This trade-off was deemed worthwhile because, in the ultra-high-resolution acquisition mode of the PCD CT with the software

version available at the time of this study, there were no spectral results to necessitate spectral optimization.

In conclusion, a clinical photon-counting detector (PCD) CT in ultra-high-resolution mode with and without deep learning noise reduction algorithm demonstrated superior performance in showing multiple myeloma lesions relative to energy-integrating detector CT. Longitudinal studies in select disease cohorts would determine the clinical impact of PCD technology in managing multiple myeloma and its precursor states.

Author contributions: Guarantors of integrity of entire study, **F.I.B., N.R.H., A.F.**; study concepts/study design or data acquisition or data analysis/interpretation, all authors; manuscript drafting or manuscript revision for important intellectual content, all authors; approval of final version of submitted manuscript, all authors; agrees to ensure any questions related to the work are appropriately resolved, all authors; literature research, **F.I.B., A.F., S.L., J.G.F.**; clinical studies, **F.I.B., N.R.H., A.F., K.N.G., S.K., J.M.C., S.L., J.G.F.**; experimental studies, **N.R.H., A.F., K.R., J.G.F.**; statistical analysis, **A.F., N.B.L., J.G.F.**; and manuscript editing, all authors

Disclosures of conflicts of interest: **F.I.B.** No relevant relationships. **N.R.H.** Patents from Mayo Clinic. **A.F.** No relevant relationships. **K.R.** No relevant relationships. **K.N.G.** Board member of International Society of CT. **N.B.L.** No relevant relationships. **S.K.** Research funding from Abbvie, Amgen, Allogene, AstraZeneca, BMS, Carsgen, GSK, Janssen, Novartis, Roche-Genentech, Takeda, Regeneron, Molecular Templates; consulting/advisory board membership with Abbvie, Amgen, BMS, Janssen, Roche-Genentech, Takeda, AstraZeneca, Bluebird Bio, Epizyme, Secura Biotherapeutics, Monterosa Therapeutics, Trillium, Loxo Oncology, K36, Sonofi, ArcellX, Oncopeptides, Beigene, Antengene, GLH Pharma. **J.M.C.** No relevant relationships. **S.L.** Royalties and licenses from Siemens Healthineers; patents from Mayo Clinic. **E.R.S.** Employee of Siemens Medical Solutions. **C.H.M.** Grant to institution from Siemens Healthineers; in-kind support from Siemens Healthineers; royalties and licenses from Siemens Healthineers; patents from Mayo Clinic; vice-president of ISCT; chair of the board, AAPM; receipt of equipment from Siemens Healthineers. **J.G.F.** Grant to institution from Siemens Healthineers.

References

1. Kyle RA, Gertz MA, Witzig TE, et al. Review of 1027 patients with newly diagnosed multiple myeloma. *Mayo Clin Proc* 2003;78(1):21–33.
2. Gleeson TG, Moriarty J, Shortt CP, et al. Accuracy of whole-body low-dose multidetector CT (WBLDCT) versus skeletal survey in the detection of myelomatous lesions, and correlation of disease distribution with whole-body MRI (WBMRI). *Skeletal Radiol* 2009;38(3):225–236.
3. Hur J, Yoon CS, Ryu YH, Yun MJ, Suh JS. Efficacy of multidetector row computed tomography of the spine in patients with multiple myeloma: comparison with magnetic resonance imaging and fluorodeoxyglucose-positron emission tomography. *J Comput Assist Tomogr* 2007;31(3):342–347.
4. Hillengass J, Usmani S, Rajkumar SV, et al. International myeloma working group consensus recommendations on imaging in monoclonal plasma cell disorders. *Lancet Oncol* 2019;20(6):e302–e312.
5. Mouloupoulos LA, Koutoulidis V, Hillengass J, et al. Recommendations for acquisition, interpretation and reporting of whole body low dose CT in

- patients with multiple myeloma and other plasma cell disorders: a report of the IMWG Bone Working Group. *Blood Cancer J* 2018;8(10):95.
6. Rajkumar SV, Dimopoulos MA, Palumbo A, et al. International Myeloma Working Group updated criteria for the diagnosis of multiple myeloma. *Lancet Oncol* 2014;15(12):e538–e548.
7. Hemke R, Yang K, Husseini J, Bredella MA, Simeone FJ. Organ dose and total effective dose of whole-body CT in multiple myeloma patients. *Skeletal Radiol* 2020;49(4):549–554.
8. Flohr TG, Stierstorfer K, Süß C, Schmidt B, Primak AN, McCollough CH. Novel ultrahigh resolution data acquisition and image reconstruction for multi-detector row CT. *Med Phys* 2007;34(5):1712–1723.
9. Leng S, Bruesewitz M, Tao S, et al. Photon-counting Detector CT: System Design and Clinical Applications of an Emerging Technology. *RadioGraphics* 2019;39(3):729–743.
10. Leng S, Yu Z, Halaweish A, et al. Dose-efficient ultrahigh-resolution scan mode using a photon counting detector computed tomography system. *J Med Imaging (Bellingham)* 2016;3(4):043504.
11. Leng S, Rajendran K, Gong H, et al. 150- μ m Spatial Resolution Using Photon-Counting Detector Computed Tomography Technology: Technical Performance and First Patient Images. *Invest Radiol* 2018;53(11):655–662.
12. Rajendran K, Petersilka M, Henning A, et al. First Clinical Photon-counting Detector CT System: Technical Evaluation. *Radiology* 2022;303(1):130–138.
13. Huber N, Anderson T, Missert A, et al. Clinical evaluation of a phantom-based deep convolutional neural network for whole-body-low-dose and ultra-low-dose CT skeletal surveys. *Skeletal Radiol* 2022;51(1):145–151.
14. Baffour FI, Glazebrook KN, Kumar SK, Broski SM. Role of imaging in multiple myeloma. *Am J Hematol* 2020;95(8):966–977.
15. Ormond Filho AG, Carneiro BC, Pastore D, et al. Whole-Body Imaging of Multiple Myeloma: Diagnostic Criteria. *RadioGraphics* 2019;39(4):1077–1097.
16. Lecouvet FE, Vande Berg BC, Malgheem J, Maldague BE. Magnetic resonance and computed tomography imaging in multiple myeloma. *Semin Musculoskelet Radiol* 2001;5(1):43–55.
17. Kumar S, Paiva B, Anderson KC, et al. International Myeloma Working Group consensus criteria for response and minimal residual disease assessment in multiple myeloma. *Lancet Oncol* 2016;17(8):e328–e346.
18. Grunz JP, Huflage H, Heidenreich JF, et al. Image Quality Assessment for Clinical Cadmium Telluride-Based Photon-Counting Computed Tomography Detector in Cadaveric Wrist Imaging. *Invest Radiol* 2021;56(12):785–790.
19. Inai R, Nakahara R, Morimitsu Y, et al. Bone microarchitectural analysis using ultra-high-resolution CT in tiger vertebra and human tibia. *Eur Radiol Exp* 2020;4(1):4.
20. Rajendran K, Petersilka M, Henning A, et al. Full field-of-view, high-resolution, photon-counting detector CT: technical assessment and initial patient experience. *Phys Med Biol* 2021;66(20):205019.
21. Hernandez AM, Wu P, Mahesh M, Siewersden JH, Boone JM. Location and direction dependence in the 3D MTF for a high-resolution CT system. *Med Phys* 2021;48(6):2760–2771.
22. Sartoretto T, Landsmann A, Nakhostin D, et al. Quantum Iterative Reconstruction for Abdominal Photon-counting Detector CT Improves Image Quality. *Radiology* 2022;303(2):339–348.